

Characterisation of thin film CdS/CdTe solar cells using electron and optical beam induced current

S.A. Galloway¹, P.R. Edwards, K. Durose*

Department of Physics, University of Durham, South Road, Durham DH1 3LE, UK

Received 10 October 1996; received in revised form 1 August 1998

Abstract

Thin-film CdS/CdTe solar cells have been imaged by EBIC and OBIC in a solar irradiation (front-wall) geometry. At low levels of injected carrier density, comparable to those due to solar irradiation, the image contrast was very low, indicating that the grain boundaries in the CdTe are electrically passivated. Further OBIC and EBIC experiments were performed as a function of injection density to investigate this in detail. The onset of unusual bright grain boundary contrast at a threshold beam current, and its decline at a very high beam currents, is interpreted in terms of the onset of high injection conditions. This, together with back- and side-wall EBIC images gives an indication of the majority carrier distribution in the CdTe. We infer that there is an enhanced concentration of holes in the vicinity of grain boundaries. That this would cause majority carriers to be repelled from the grain boundaries is consistent with our direct observation of grain boundary passivation: hence detailed quantitative EBIC studies have enabled an electrical mechanism of grain boundary passivation in CdS/CdTe solar cells to be postulated. © 1999 Elsevier Science B.V. All rights reserved.

Keywords: CdS/CdTe; EBIC; Grain boundary passivation

1. Introduction

Thin film CdS/CdTe solar cells comprising layers of CdTe/CdS/TCO/glass are well known as a favoured technology for large area, low-cost photovoltaic energy conversion. Indeed at the time of writing such cells are nearing large-scale production by several

* Corresponding author. E-mail: ken.durose@durham.ac.uk

¹ Now at: Oxford Instruments Ltd., Tubney Woods, Abingdon, Oxfordshire OX13 5QX, UK.

manufacturers [1]. Research scale devices have been demonstrated with efficiencies of up to 16.0% [2] and have good stability. The materials are robust enough to enable processing by close space sublimation, electrochemical and other means. Nevertheless, good control of deposition and contacting to these polycrystalline structures is insufficient to produce high-efficiency devices, and some form of chloride ion treatment is necessary to effect doping of the CdTe. The effects of chloride treatment and annealing are the subject of much literature. Increases in V_{oc} , J_{sc} and η , promotion of grain growth and interdiffusion are all described. It is known that the treatment changes the dominant current transport mechanism from interface recombination/tunnelling to thermally activated thus suggesting a decrease in the density and dominance of interface states [3–5]. It has also been suggested that the treatment passivates grain boundaries and this is certainly consistent with the high efficiencies achieved from these thin film devices in which the grain size is of the order of 0.1–10 μm .

Grain boundaries and microstructures have been studied by, for example, SEM and XRD in order to relate structure to performance [6,7]. Higher resolution studies by AFM [4] and TEM [8,9] have also been undertaken. However, in order to understand carrier generation and collection at a microscopic level, beam injection techniques should be used. Moreover, the carrier injection should be done in a geometry relevant to solar injection while having sufficient resolution to probe grain boundaries. Examination of CdS/CdTe solar cells while attached to their ITO/glass substrates presents some limitations in this respect. Excitation with a focused laser beam through the glass limits the resolution which has so far been obtained with OBIC (optical beam-induced current) to 2–4 μm [10]. Although EBIC microscopy (electron beam-induced current) affords higher spatial resolution the glass prevents injection in the solar irradiation geometry, i.e. through the device's front wall.

In this paper front-wall injection EBIC experiments are reported in which the glass was first removed by an etch-stop method. It was also observed that the EBIC and OBIC collection efficiency of these devices decreased at a threshold of optical or electron injection density much greater than that corresponding to solar irradiation. This onset of “high injection conditions” was used to provide an indication of equilibrium carrier density on a sub-micron scale. Hence, by varying the injection density the electrical properties of the grain boundaries could be differentiated from the grains. This allowed a mechanism for grain boundary passivation to be postulated for this material.

2. Experimental procedure

2.1. Solar cell fabrication and the beam injection experiments

The cells studied were fabricated by ANTEC GmbH and comprised $\sim 8 \mu\text{m}$ of CdTe deposited on ~ 100 – 200 nm of CdS, itself deposited on ITO coated glass substrates. While the CdTe was deposited by close space sublimation (CSS) at 500°C , the CdS was deposited by either physical vapour deposition (PVD) at 150°C or CSS at

500°C. CdCl_2 treatment was done by evaporating a 60 nm layer of CdCl_2 onto the CdTe, followed by annealing in air for 25 min at 400°C. A control device (referred to as “heat-treated”) was prepared by annealing a device under the same conditions but without first applying CdCl_2 . While the CdCl_2 treated devices were 10.5–11% efficient, the heat-treated ones were $\sim 3\%$ efficient. For further details of previous work concerning structural, spectral and optical characterisation of solar cells manufactured by ANTEC GmbH the reader is referred to the following Refs. [1,8,10–14].

The novel aspect of this work arises from the comparison of the beam injection microscopy images and behaviour of the cells when probed using different beam injection geometries as shown in Fig. 1. OBIC can be measured by illumination through the glass but for EBIC the glass was removed by grinding it to a thickness of $\sim 100\text{ }\mu\text{m}$. After making a back contact to the CdTe the remaining glass was removed with HF. The ITO acts as an etch-stop layer. Other surfaces can be masked with Lacomit varnish leaving the ITO free for contacting with a gold wire attached by silver dag.

For back-wall EBIC it was essential to polish flat the surface morphology arising from polycrystallinity in order to eliminate its influence on the measurements [12]. This was done using a fine grade diamond paste followed by etching in 0.5% bromine in methanol for 3 min. Typically this left approximately $4\text{ }\mu\text{m}$ of CdTe which was contacted by evaporating gold.

The OBIC system is described elsewhere [10,11]. Briefly it comprises a He–Ne laser focused onto the junction through the glass substrate by a long working distance objective. An OBIC image is obtained by piezo-electric rastering of the specimen with respect to the beam and measuring the short circuit current using a lock-in amplifier. Optical filters were used to adjust the intensity of the focused laser illumination.

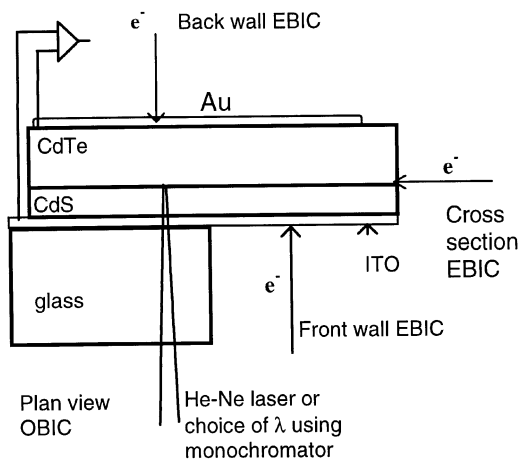


Fig. 1. Schematic representation of the solar cell structure and the different geometries for injecting carriers using OBIC and EBIC. Front-wall EBIC can only be performed after removal of the glass substrate.

EBIC microscopy was performed in a JSM IC-848 SEM fitted with an Oxford Instruments CF301 cold stage. The EBIC was measured using a Matelect ISM5 DC amplifier which was calibrated to a PC-based frame grabber capable of signal averaging.

2.2. Determination of valid beam injection conditions for EBIC experiments

In order to perform meaningful EBIC experiments it was necessary to ensure that the experimental carrier injection conditions corresponded as closely as was practical to those encountered under normal device operation, i.e. to relate the electron beam injection rate to that of sunlight. Depth-dosage profiles were therefore calculated for an abrupt CdS (100 nm)/CdTe structure using both an AM1.5 solar spectrum and electron beams of varying accelerating voltages. For the optical work the AM1.5 spectral data given by Fahrenbruch [15] was used and the dosage calculated by integrating the absorption with radiance as a function of wavelength. The resulting curve (Fig. 2a) shows that the majority of the carriers are generated in the first half micron of the absorber. It is worth noting that the depth dependence of carrier generation which results from using a He–Ne laser ($\lambda = 633$ nm) in the OBIC experiments is slightly biased in favour of greater depths compared to using white light illumination.

The depth-dosage profile for EBIC experiments was modelled by Monte–Carlo simulations [16]. In order to match the experiments, injection into a structure comprising ITO (50 nm)/CdS (100 nm)/CdTe (10 μm) was modelled. Since carrier generation is a complicated function of both the radius and depth from the point of incidence, some approximations were necessary to obtain the average dosage as a function of depth. In this work all generation outside a cylinder concentric with the beam and of diameter equal to half the Grün range was ignored, and inside the cylinder the generation rate was assumed to be uniform. The errors in this approach are at a maximum when close to the point of incidence where the generation rate is concentrated at the centre of the cylinder. This method was used in preference to recording the maximum generation rate as a function of depth because the spiked

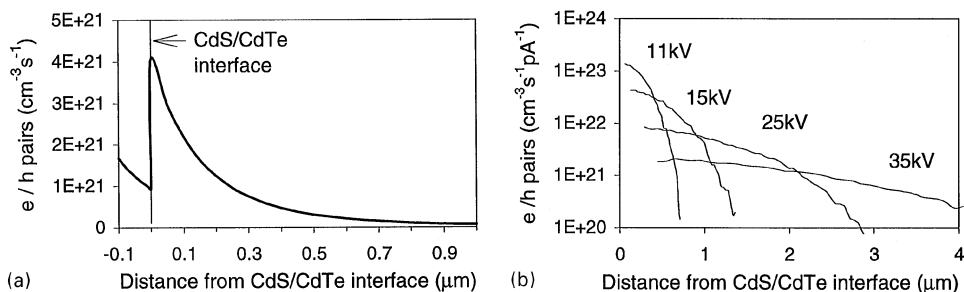


Fig. 2. Calculated depth-dose profiles for carrier injection in ITO (50 nm)/CdS (100 nm)/CdTe (10 μm): (a) For AM1.5 illumination; and (b) For electron beams of current 1 pA and of variable accelerating voltage. The units are electron/hole pairs generated/ cm^3 .

nature of the generation function would lead to a large overestimation of the generation density. Fig. 2b shows the resulting depth-dosage profiles as a function of the accelerating voltage for a beam current of 1 pA. The dosage is not given for the window and near-surface regions where the errors mentioned above are significant. The best fit between depth profile of solar and electron beam irradiation is achieved by using an accelerating voltage of 11 kV. However, to match the generation density using this voltage requires an incident beam current of much less than 1 pA. At this low beam current difficulties are to be expected in the recording of SEM/EBIC images. For the front-wall EBIC experiments reported here an accelerating voltage of 11 kV and a variable beam current ($5 \times 10^{-13} - 5 \times 10^{-9}$ A) were used.

3. Results

3.1. OBIC images and measurements

OBIC images and signals were obtained from the CdCl_2 and heat-treated cells as a function of incident beam power. In all cells the collection efficiency and image contrast were found to depend strongly on the power of the incident beam, particularly at high powers. Fig. 3a shows images recorded from a CdCl_2 -treated cell using focused beam powers of (a) 0.1 W cm^{-2} , i.e. close to the normal working conditions of AM1.5 and (b) 10 W cm^{-2} . The images may be considered as maps of short circuit current density with bright corresponding to high, and dark to low regions of current collection. Even though for these images the contrast was enhanced by a factor of $\times 10$ and the brightness optimised to reveal detail, Fig. 3a (low laser intensity) has very low image contrast. This indicates very uniform collection efficiency. An image recorded at intermediate beam power density ($\sim 1 \text{ W cm}^{-2}$) confirmed that the low image contrast was not an artefact due to low beam currents. Moreover, images comparable to that in Fig. 3b in which dark areas $5\text{--}10 \mu\text{m}$ in size were present were only observed at high injection density levels. Such areas indicate poor carrier collection efficiency.

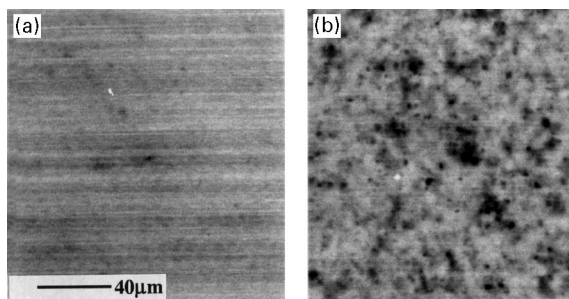


Fig. 3. OBIC images obtained for a CdCl_2 -treated cell using focused He–Ne light with: (a) 0.1 W cm^{-2} ; and (b) 10 W cm^{-2} of incident power. Strong contrast (as in b) only arises at incident power densities much higher than that of solar irradiation.

To investigate this effect in more detail the short circuit response (i.e. OBIC) excited by a stationary focused beam as a function of the laser beam power was recorded for good and poor areas on both the CdCl_2 and heat-treated cells. The results are plotted as OBIC normalised to the beam power in Fig. 4. Both specimens show a similar trend with a high response plateau at low power which falls substantially as the irradiance power is increased over several orders of magnitude. In addition, the contrast (response difference) between good and poor areas is always the least in the low intensity regime, increases substantially in the mid-intensity regime and reduces somewhat in the high intensity regime. In all cases the CdCl_2 -treated cell shows better collection efficiency than any of the best performing areas of the heat-treated cell. It is this threshold behaviour of the beam injection response which is interpreted in terms of the onset of “high injection” conditions in EBIC imaging in Section 4.

3.2. Front-wall EBIC results

Front-wall EBIC images of a CdCl_2 -treated cell recorded using beam currents of (a) 1 nA and (b) 0.5 pA at 11 kV are shown in Fig. 5. (For these images the intensity convention is the same as for the OBIC images presented earlier, i.e. bright contrast corresponds to good, and dark to poor carrier collection). The two images are taken from a series recorded using beam currents varying from 0.5 pA to 5 nA and are typical for those seen under conditions of high and low carrier injection density, respectively. Both have been contrast enhanced to the same degree.

Under high injection conditions (Fig. 5a) there is a contrast in which dark regions 2–3 μm in size are surrounded by a network of bright regions. From CdTe grain size measurements on the same cells it is reasonable to assume that the dark features correspond to grains while the bright features correspond to grain boundaries in the CdTe. It is also known from Monte–Carlo simulations of injection density that this type of contrast only arises for injection density many times greater than that of

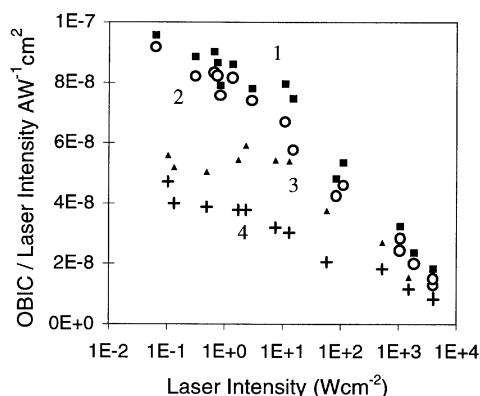


Fig. 4. Ratio of OBIC signal to light beam intensity (collection efficiency) from: (1) CdCl_2 -treated cell – good area; (2) CdCl_2 -treated cell – poor area; (3) Heat-treated cell – good area; and (4) Heat-treated cell – poor area.

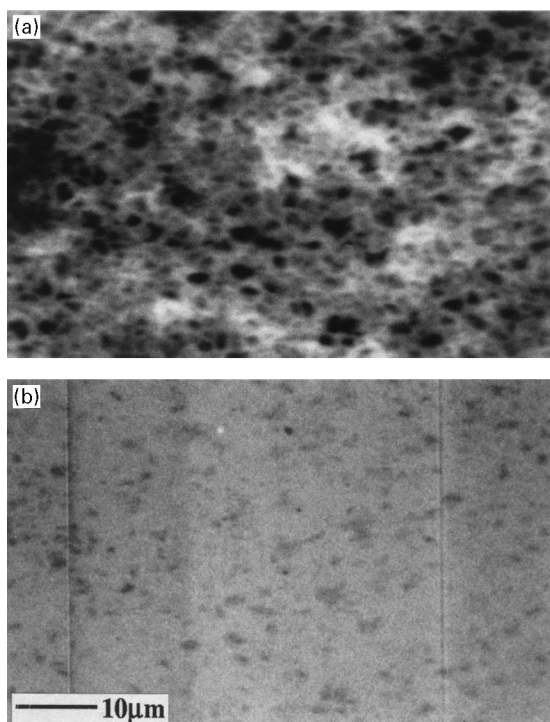


Fig. 5. Front-wall injection EBIC images recorded at 11 kV from a CdCl_2 -treated cell: (a) Beam current = 1 nA. Dark grain and bright grain boundary contrast is visible; and (b) Beam current = 0.5 pA. There are no specific contrast features. (The vertical lines are due to interference from the SEM scan generator).

AM1.5 illumination. It can therefore be said that *for these injection conditions* the collection efficiency of the grain interiors is lower than that of the grain boundary regions. This is the opposite of what is expected for the case of enhanced recombination at grain boundaries.

The lower injection conditions of Fig. 5b are more comparable to the conditions of solar irradiation. Although enhanced to the same degree as Fig. 5a, the contrast of this image is much reduced and grain boundary features are not visible. This indicates that the collection efficiency is very uniform indeed and there is, for example, no especially strong recombination at grain boundaries under these injection conditions.

As for the OBIC response, the variation in contrast of EBIC images of the CdCl_2 -treated solar cell with beam current was investigated in more detail. However, while for the measurements of OBIC efficiency versus beam power were plotted for a stationary beam (Fig. 4), in the case of the EBIC the average contrast was extracted from the digitised EBIC images and plotted against beam current (I_{beam}) as shown in Fig. 6. To achieve this the EBIC signal from each pixel was plotted on a histogram. The full-width half-maximum was taken as the average spread. The average contrast

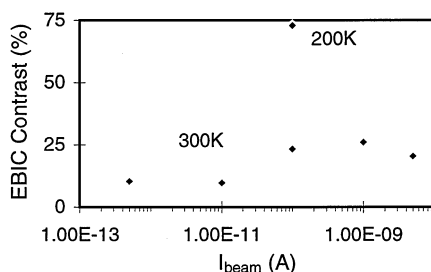


Fig. 6. Average contrast of front-wall EBIC images as a function of I_{beam} at 11 kV. The contrast is high for $10^{-11} \text{ A} < I_{\text{beam}} \leq 10^{-9} \text{ A}$ and is low for beam currents above and below this range.

was then calculated by normalising the spread to the EBIC signal at the peak of the distribution. The results are shown in Fig. 6 in which it can be seen that the average contrast is at a low value ($\sim 10\%$) until a high electron beam current is reached ($\sim 10^{-10} \text{ A}$), whereupon the contrast increases substantially. The contrast then falls again as the beam current is increased to very high levels ($\sim 5 \times 10^{-9} \text{ A}$) – a behaviour which was reproducible for a number of samples and which accords with the OBIC results of Fig. 4 (note that in Fig. 4 the contrast is related to the difference between the two curves).

Further front-wall imaging was performed at 200 K and Fig. 6 has one point corresponding to the contrast measured ($\sim 70\%$) in the mid-injection current regime. The contrast was, however, of the same form as in Fig. 5a (bright grain boundaries) and this is a point of some relevance to the comparisons of the other EBIC experiments made in the discussion of contrast in Section 4.

It is central to the analysis of the injection-dependent contrast effects reported here to discriminate between effects due to the variation in the level of carrier injection (i.e. I_{beam} in EBIC) and due to carrier injection *density*. To this end modelling of a simple solar cell equivalent circuit, and additional EBIC experiments were undertaken. In the modelling work a circuit comprising a p–n junction with shunt and series resistances was used to show that the measured current flowing in the circuit can be a complicated function of the current supplied by a current source. The shape of the response is a strong function of the series resistance. Hence, the variation in collection efficiency of the solar cells with injected current is a possible explanation for the OBIC versus beam power shown in Fig. 4.

It is only by varying the injection current and injection current density independently in EBIC experiments that the dominant variable was identified as injected carrier density. SEM/EBIC affords two means of varying the injection density: either the beam current may be increased at constant accelerating voltage or the voltage (and hence generation volume) may be increased for constant beam current. Both methods were used in this work, but as both indicate the same conclusions only the variation of I_{beam} will be described here. The measure of EBIC collection efficiency used was the EBIC normalised by the beam power, $\text{EBIC}/[I_{\text{beam}} \times V]$, where V is the accelerating voltage. (This is proportional to collection efficiency if losses due to

electron backscattering for example are not a function of injection conditions.) Normalised EBIC was recorded as a function of I_{beam} for voltages of 15, 25 and 35 kV while scanning at TV rate, as shown in Fig. 7. The curves show behaviour which changes after a threshold of injection density is exceeded. At 35 kV a distinct plateau is seen for $I_{\text{beam}} \leq \sim 3 \times 10^{-10}$ A. Above this the normalised EBIC declines logarithmically. Similar behaviour is seen for 15 and 25 kV but the turning points are at lower values of I_{beam} . This is interpreted as being because the threshold injection density is exceeded for lower I_{beam} when the generation volume is smaller. Complementary results were obtained by varying the accelerating voltage at constant I_{beam} , confirming that the contrast effects of Fig. 5 are injection current density dependent.

3.3. Back-wall and cross-section EBIC results

Fig. 8 shows back-wall EBIC images of a CdCl_2 -treated cell taken at 200 and 300 K with an accelerating voltage of 25 kV and with $I_{\text{beam}} = 0.5$ nA. At room temperature the grain boundaries are difficult to distinguish from the general contrast ($\sim 70\%$). However, cooling makes the boundaries more distinguishable as dark contrast features. This is an inversion of the bright contrast seen in front-wall EBIC, an observation of some importance to the discussion. Also it is the case that back-wall EBIC micrographs show a much greater degree of inhomogeneity in the CdTe than does front-wall EBIC. This must indicate the presence of recombination centres located in parts of the device which have little influence on its normal operation, i.e. deep in the CdTe away from the collecting junction. This can lead to some uncertainty in the validity of the results of back-wall injection EBIC experiments.

Cross-section EBIC experiments were performed in order to further investigate the temperature-dependent contrast effects. EBIC linescans were recorded for the same

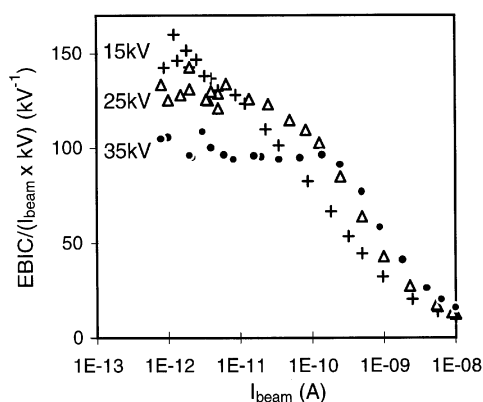


Fig. 7. Normalised EBIC versus I_{beam} at 15, 25 and 35 kV. The EBIC efficiency starts to decline at a threshold value of I_{beam} which is lower for lower values of accelerating voltage. This indicates that the response is related to injection current density rather than injection current (see text).

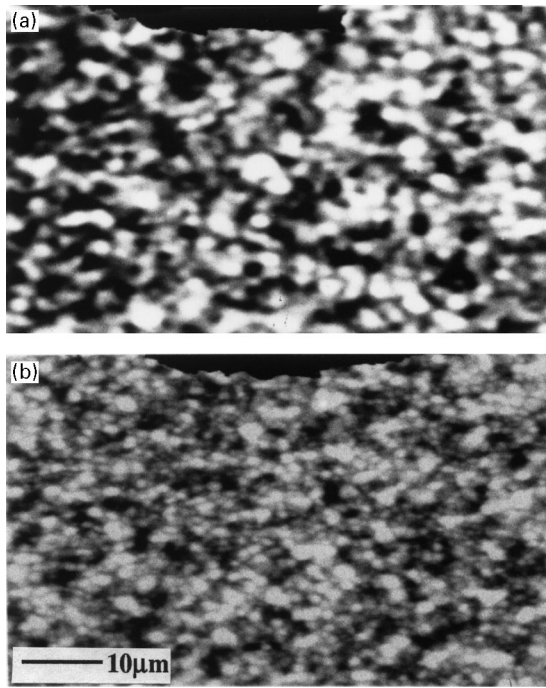


Fig. 8. Back-wall EBIC taken at 25 kV with $I_{\text{beam}} = 0.5 \text{ nA}$ at: (a) 300 K; and (b) 200 K. The dark regions representative of grain boundaries are more distinct at low temperatures.

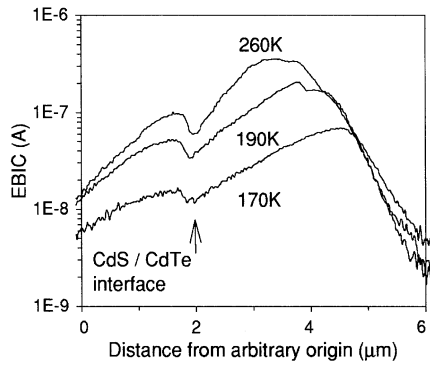


Fig. 9. Cross-section EBIC linescans from CdS/CdTe showing the movement of peak collection efficiency away from the metallurgical junction with reduced temperature.

area between 170 and 260 K as shown in Fig. 9. The collection efficiency falls, and the position of maximum collection moves toward the back contact (away from the CdS/CdTe interface) with decreasing temperature. This is likely to be caused by carrier freeze-out, suggesting the acceptors to be relatively deep.

The shape of the $\ln(\text{EBIC})$ versus distance plot (Fig. 9) gives an estimate of the minority carrier diffusion length L_n , subject to the usual approximation. Between room temperature and 170 K, L_n was measured to decrease from 0.5–0.33 μm . This data indicates that previous conclusions about the temperature dependence of L_n made by the authors and based on back-wall EBIC observations are in error [10,11].

4. Discussion

The observation of very low OBIC and EBIC contrast for front-wall injection at low beam powers is direct evidence of grain boundary passivation. Areas of significant recombination would be visible as dark contrast but grain boundaries are not visible as such in any of the front-wall micrographs. However, comparison of the dark grain boundary contrast seen in back-wall EBIC and the bright grain boundary contrast seen at high injection density front-wall EBIC is, at first sight, not self-consistent. A simple interpretation in terms of high and low recombination strengths of the grain boundaries is not appropriate. Hence, an alternative explanation of the contrast inversion should be sought which explains all of the observations.

The concept of high and low injection conditions is central to the interpretation of the observed contrast effects. Conditions of high carrier collection are said to prevail when the density of beam injected carriers exceeds the density of majority carriers in the semiconductor. Under high injection conditions the carriers move under the influence of the local concentration gradient of non-equilibrium carriers [17] and this acts to reduce the EBIC collection efficiency. This effect can be seen in Fig. 7. The injection density at which the normalised EBIC signal begins to fall from its plateau represents the transition from low to high injection conditions and can, in principle, be related to the material's majority carrier concentration [18]. However, to do this significant approximations must be made since the carrier concentration is non-uniform and the processes of drift and diffusion are a strong function of depth in this thin film device. An order of magnitude estimate was obtained from the injection current threshold of $I_{\text{beam}} = 200 \text{ pA}$ (Fig. 7) at 35 kV, for which the average dose is $2 \times 10^{21} \text{ cm}^{-3} \text{ s}^{-1} \text{ pA}^{-1}$ (Fig. 3). Using $n = g\tau$ and $\tau = 2 \times 10^{-9} \text{ s}$ [19] gives an injected carrier concentration of $8 \times 10^{14} \text{ cm}^{-3}$. This compares well with our estimate of $4.2 \times 10^{14} \text{ cm}^{-3}$ obtained from C–V measurements of the same cells.

In order to explain the dependence of the grain boundary contrast on injection conditions we make use of the observation that EBIC collection efficiency is reduced on reaching high injection conditions. Since contrast represents a local difference in EBIC collection, contrast due solely to the injection density effect must arise from local differences in the threshold beam current for high injection conditions. This would be due to local differences in equilibrium carrier density. Since the front-wall low injection images have low contrast we make the assumption that the contrast at high injection is dominated by the effects of high injection and not by recombination. According to this model the contrast in Fig. 6 may be explained as follows:

(a) Low I_{beam} ($I_{\text{beam}} \leq 10^{-11} \text{ A}$). Low injection conditions prevail and low contrast indicates that grain boundaries are passivated.

(b) Medium I_{beam} ($10^{-11} \text{ A} < I_{\text{beam}} \leq 10^{-9} \text{ A}$). Bright grain boundary contrast is visible. The grains are considered to be at high injection and the grain boundaries at low injection, hence decreasing the EBIC collection efficiency of the grain interiors with respect to the grain boundaries. This implies that the equilibrium carrier concentration near the grain boundaries is higher than in the grains.

(c) High I_{beam} ($I_{\text{beam}} > 10^{-9} \text{ A}$). The grain boundary contrast decreases with further beam current increases indicating that both the grains and the boundaries are reaching conditions of high injection. The EBIC collection efficiencies of both the grains and their boundaries decline and become more equal. This implies that the equilibrium carrier concentration first at the grains and now at the grain boundaries is exceeded by the injected carrier density.

From the above arguments it may be inferred that the CdTe grain boundaries have a higher local carrier density than the grains. Furthermore, since the p-type doping is effected by CdCl_2 -treatment from the back-wall of the cell it might be expected that there is a carrier concentration gradient from the back to the front of the cell. This suggests the carrier density profile sketched in Fig. 10a. From this carrier distribution it might be expected that near to grain boundaries the p–n junction is positioned more closely to the metallurgical junction than it is in the bulk of a grain. This being so, at all positions the junction would remain accessible to the generation volume for front-wall injection. However, since the CdTe is thick, carriers injected through the back-wall by an electron beam might only be collected when the junction is positioned sufficiently close to the deepest extent of the generation volume. Even for high accelerating voltages collection is only good from the grains which are then revealed

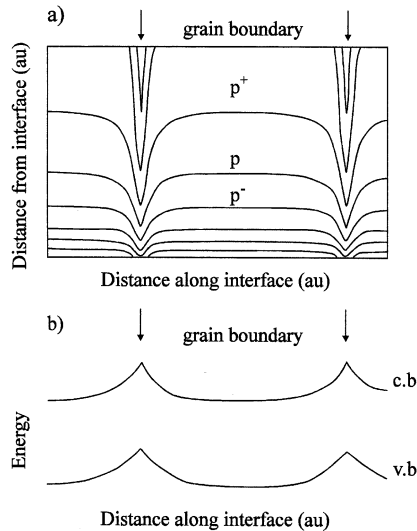


Fig. 10. (a) Carrier density distribution contour map and (b) band diagram for near grain boundary regions and consistent with the EBIC observations reported in this work. Minority carriers (electrons) are expected to be repelled by the grain boundaries, making recombination there less probable.

by bright contrast (Fig. 8a). Cooling reduces the carrier concentration, moving the p–n junction towards the back-wall (Fig. 9). More of each grain is therefore revealed as bright contrast and this apparently exposes the grain boundaries as dark contrast.

All of the EBIC observations are consistent with the carrier density distribution contour plot in Fig. 10a. Such a distribution could arise from (a) trapped negative charge at the grain boundaries causing positive band bending and a surrounding accumulation region as shown in Fig. 10b and/or (b) segregation of acceptor species to the grain boundaries. A relevant example of segregation is given by Levi et al. [20], who have used Auger microscopy to demonstrate segregation of Te to the grain boundaries after certain contacting procedures.

Postulation of an enhanced hole concentration near the grain boundaries is consistent with the repulsion of minority carriers (holes) in the CdTe. This work therefore suggests a mechanism of grain boundary passivation in CdS/CdTe solar cells.

5. Conclusions

Removal of the glass substrate from CdS/CdTe solar cells has enabled front-wall injection EBIC to be performed and compared to high-resolution OBIC for the first time. At injection levels comparable to those due to solar radiation the uniformity of the images provides the first direct microscopic evidence of grain boundary passivation in these cells.

Understanding of the injection level dependence of image contrast in front-wall injection EBIC suggests a model for charge distribution near to grain boundaries in the CdTe. The unusual bright front-wall EBIC contrast and the dark back-wall contrast at grain boundaries suggest that the boundaries are associated with higher densities of majority carriers (holes) than the grains themselves. This could be due to either an accumulation layer or segregation of acceptors and is consistent with there being minority carrier repulsion from the grain boundaries. The charge distribution model proposed therefore represents a mechanism of grain boundary passivation in CdS/CdTe solar cells.

Acknowledgements

The authors wish to thank ANTEC GmbH for the samples, Dr. P.R. Wilshaw, of Oxford University for access to the OBIC apparatus, and Dr. A.W. Brinkman for useful discussions.

References

- [1] D. Bonnet, Proc. 14th European PVSEC, Barcelona, 1997, p. 2688.
- [2] T. Aramoto, S. Kumusawa et al., *Jpn. J. Appl. Phys.* 36 (1997) 6304.

- [3] S.A. Ringel, A.W. Smith, M.H. MacDougal, A. Rohatgi, *J. App. Phys.* 70 (1991) 881.
- [4] H.R. Moutinho, F.S. Hasoon, L.L. Kazmerski, *Prog. Photovoltaics* 3 (1995) 39.
- [5] A. Rohatgi, *Int. J. Sol. Energy* 12 (1992) 37.
- [6] T.X. Zhou, N. Reiter, R. Powell, R. Sasala, P.V. Meyers, *Proc. 1st WCPEC, Hawaii, 1994*, p. 103.
- [7] A.N. Tiwari, K. Kessler, V. Vorlicek, V. Zelezny, M. Krejci, S. Blunier, H. Zogg, *Proc. 13th European PVSEC, 1995*, p. 2051.
- [8] Y.Y. Loginov, K. Durose, H.M. Al-Allak, S.A. Galloway, S. Oktik, A.W. Brikman, H. Richter, D. Bonnet, *J. Crystal Growth* 161 (1996) 159.
- [9] M.M. Al-Jassim, F.S. Hasoon, K.M. Jones, B.M. Keyes, R.J. Matson, H.R. Moutinho, *Proc. 23rd IEEE Photovoltaic Specialists Conf. 1993*, p. 459.
- [10] S.A. Galloway, A.W. Brinkman, K. Durose, P.R. Wilshaw, A.J. Holland, *App. Phys. Lett.* 68 (1996) 3725.
- [11] S.A. Galloway, A.J. Holland, P.R. Wilshaw, A.W. Brinkman, K. Durose, *Proc. 13th European PVSEC, Niece, 1995*, p. 2072.
- [12] S.A. Galloway, K. Durose, *Inst. Phys. Conf. Ser.* 146 (1995) 709.
- [13] G. Stollwerck, J.R. Sites, *Proc. 13th European PVSEC, Nice, 1995*, p. 2020.
- [14] H.M. Al-Allak, A.W. Brinkman, H. Richter, D. Bonnet, *J. Crystal Growth* 159 (1996) 910.
- [15] A.L. Fahrenbruch, R.H. Bube, *Fundamentals of Solar Cells; Photovoltaic Solar Energy Conversion*, Academic Press, New York, 1983.
- [16] D.B. Holt, D.C. Joy, *SEM Microcharacterisation of Semiconductors*, Academic Press, London, 1989.
- [17] S.M. Sze, *Physics of Semiconducting Devices*, Wiley, New York, 1981.
- [18] V.P. Singh, R.H. Kenney, J.C. McClure, S.P. Albright, B. Ackerman, J.F. Jordan, *Proc. 19th IEEE Photovoltaic Specialists Conf., 1987*, p. 216.
- [19] R.K. Ahrenkiel, B.M. Keyes, D.L. Levi, K. Emery, T.L. Chu, S.S. Chu, *Appl. Phys. Lett.* 64 (1994) 2879.
- [20] D.H. Levi, L.M. Woods, D.S. Albin, T.A. Gessert, D.W. Nilas, A. Swartzlander, D.H. Rose, R.K. Ahrenkiel, P. Sheldon, *Proc. 26th IEEE Photovoltaic Specialists Conf., Anaheim, CA, 1997*, p. 351.